

Effect of Passivation on Properties and Performance of Perovskite Solar Cells

Radwa Esmael^{1, 2}, Hassanin El-Labany¹, Shaker Ebrahim³,
Ayman El-Tahan^{1*}

¹Physics Department, Faculty of Science, Tanta University, P.O. Box: 44519, Tanta, Egypt.

²Higher Institute of Engineering and Technology, P.O. Box: 31739, Egypt.

³Department of Materials Science, Institute of Graduate Studies and Research, Alexandria University, P.O. Box: 832, Alexandria, Egypt.

* Correspondent; ayman.eltahan@science.tanta.edu.eg

Perovskite solar cells (PSCs) represent one of the most models of the organic-inorganic solar cells which have achieved a great success in the last years. However, there are some of challenges facing this success such the barrier between the layers' interfaces and the presence of grains that impedes the passage of the charge carriers. Consequently, the aim of this work is to synthesize and characterize passivated perovskite layers using different passivation techniques for producing treated perovskite solar cells. These treated layers were characterized by scanning electron microscope (SEM), UV-visible spectroscopy, photoluminescence, X-ray diffraction (XRD), Fourier transform infrared (FTIR) and current density-voltage measurements. The optimal performance of the fabricated and passivated PSCs with a structure of FTO/blocking layer/mesoporous layer/TiCl₄/methylammonium (MA)PbI_{3-x}Cl_x/chlorobenzene/C had short circuit current density (*J*_{sc}), open circuit voltage (*V*_{oc}), fill factor (*FF*) and efficiency of 20 mA/cm², 0.56 V, 0.29 and 6.5 %, respectively.

1. Introduction:

The organic-inorganic lead halide perovskite solar cells (PSCs) are the most promising third generation solar cells. The power conversion efficiency (PCE) has exceeded 25% [1]. The optical and electrical advantages of the perovskite material such as low-cost, convenient fabrication techniques, largely tunable band gap (e.g., CH₃NH₃PbX₃ has a band gap from 1.5 eV to 2.3 eV) [2] and great light absorption coefficient (higher than 10⁴ cm⁻¹) [3, 4]. However, there are several challenges facing the progress of this type of solar cells such as the weak contact between the interfacial layers, high series resistance between layers, large numbers of grain boundaries in the active layer and probable degradation of the organic layer.

The passivation process refers to a material becoming passive or less corroded by the environment. Passivation involves the application of the outer layer of a shielding material as a microcoating and created by chemical reaction with the base material [5]. In the PSCs, the passivation taints to either chemical passivation, which reduces the defects trap states in order to optimize the charge transfer between various interfaces [6-10], or physical passivation, which isolates certain layers from the environment to avoid the degradation process. The self, surface and interface chemical passivation are commonly used and efficient strategies to reduce defects and improve the photovoltaic performance of PSCs [11-13].

The self-passivation was carried out by doping MAPbI₃ with Cl and it was found that 10% PbCl₂-MAPbI_{3-x}Cl_x film has a broadened bandgap which enables the sensibility to ultraviolet light to reduce defect density [14]. In addition, by applying the self-passivation method the efficiency of solar cell was increased from 1.63% (without passivation) to 4.09%. The surface passivation technique on the active layer with a non-polar solvent was intended to reduce charge recombination and improve charge transport through the layer. This had led to smoother surface perovskite films with large grains. Moreover, the chlorobenzene washing process had produced compact, larger grain size, uniform and densely-packed crystalline surface topography [15-17].

In order to ensure crystallization of the perovskite layer, using chlorobenzene (CB) as an antisolvent solution, had resulted in planar perovskite films with highly homogenous and pinhole-free, and the efficiency had increased to be 4.45%. The interface passivation method between the electron transport layer (ETL) and active layer was targeted to achieve the efficient electron-selective contacts. PSCs consist of several layers between which the charges travel among themselves, and when each layer is connected the other; it resembles a series resistance increasing the charge recombination. To overcome on this resistance, a new ETL, which had made from TiCl₄ was deposited on mesoporous TiO₂ that had been fabricated by dipping method [18]. When performing different measurements, the cell with a new layer of TiCl₄ treatment had a homogenous porosity surface suitable for perovskite infiltration, the recombination is reduced and the efficiency is increased to be 6.5% at the final of passivation series.

The objective of the presence work is to investigate the effect of different passivation techniques on the structural properties and performance of the fabricated PSCs. The hole free conventional mesoporous PSC is fabricated as a reference cell by an infiltration perovskite layer onto the carbon electrode. The PSCs are compared with and without passivation methods. The treated and passivated interfacial layers were characterized using scanning electron microscope (SEM), UV-visible spectroscopy, photoluminescence, X-ray

diffraction (XRD), and Fourier transform infrared (FTIR) and current density-voltage measurements.

2. Materials and Methods:

2.1. Materials:

Acetone (Sigma-Aldrich, 99%), chlorobenzene (Fisher Scientific, 98%), diethyl ether (Fisher Scientific, UK, 99%), dimethyl sulfoxide (DMSO) (Across, New Jersey, USA, 99.8%) have been purchased. Ethyl cellulose "EC" (HMW) (Sigma Aldrich, 48.0-49.5% (w/w) ethoxyl basis), ethyl cellulose "EC" (LMW) (Sigma Aldrich, 48.0-49.5% (w/w) ethoxyl basis), ethanolamine (Fluka, 99.5 %) have been purchased too. Fluorine doped Tin Oxide "FTO" glass substrate (Sigma-Aldrich, 13 Ω /sq.), graphite powder (Fisher Scientific, UK, Purpose Grade), hydroiodic acid, 57wt% (Across, New Jersey, USA) and isopropanol (Sigma-Aldrich, 99%) have been purchased. Lead (II) chloride (Fisher Scientific, 99%), lead (II) iodide (Fisher Scientific, 99%), methylamine (CH₃NH₂), extra pure and 40 wt% solution in water (Across, New Jersey, USA) has been bought. Titanium isopropoxide (Sigma Aldrich, 97%), titanium tetrachloride "TiCl₄" (Sigma Aldrich, 99%), alpha-terpineol 97% were as purchased from Across Organics. Acetyl acetone, 98% was obtained from Alpha Chemika and carbon black was received from carbon black Company (Alexandria, Egypt).

2.2. Preparation of TiO₂ blocking layer and TiO₂ paste

Ti isopropoxide (0.6 ml) and acetylactone (0.4 mL) were mixed and stirred for 30 min at room temperature and then this mixture was added to 9 mL absolute ethanol and stirred for 30 min at room temperature. An amount of 58.6 g (0.2 moles) of Ti isopropoxide was dissolved at once to 12 g (0.2 moles) of acetic acid and stirred at room temperature for 15 minute. Then, the precursor solution was poured into 290 mL water quickly while stirring at speed of 700 rpm. After 1 hr of stirring, 4 mL of nitric acid was added to the mixture and then heated 80°C in 40 minute and peptized for 75 min with adding the water to this solution until the final volume becomes 370 mL. The mixture solution was then kept in autoclave at 250°C for 12 hours. After this step, 2.4 mL of 65% nitric acid was added and the dispersed solution was sonicated [19-22]. The mixture was then concentrated by using rotary evaporator and to get the concentrated mixture from this solution, the organic and other solvents were removed by centrifuge and this step was repeated three times, then we dividing this mixture in many tubes and washing with ethanol many times a white precipitate containing 40wt.% TiO₂ in ethanol was obtained. Finally, TiO₂ was dried in a vacuum oven for 6 hours at 80°C and then TiO₂ was grinded using a mortar to produce a fine white powder.

There were two kinds of Ethyl Cellulose (EC) powders used in this study to prepare TiO₂ paste from EC (5-15 mPa.s) and EC (30-50 mPa.s). 45 g of the EC (5-15 mPa.s) and 35 g of the EC (30-50 mPa.s) Ethyl Cellulose powder were dissolved in ethanol to have 10wt.% solution. 16 g of the prepared TiO₂ and 64.9

g of alpha-terpineol were added to the ethanolic EC solution and diluted with 80 mL of ethanol to obtain a total volume of 280 mL. The mixture was then sonicated and stirred. Water and ethanol were removed from TiO_2 and e EC solution by rotary evaporator from initial temperature of 40°C to a final temperature at 50°C . The final paste was made with a hand mill. The final paste containing 18wt.% TiO_2 , 9wt.% EC and 73wt.% terpineol was used for both characterizations and devices fabrication. 0.04 mL of 99% TiCl_4 solution was prepared by slowly dropping TiCl_4 over 50 g DI in ice and then diluted with 250 mL DI water in a 300 mL at room temperature.

2.3. Synthesis of MAI, MAPbI_3 and $\text{MAPbI}_{3-x}\text{Cl}_x$

Both of 20 mL of methylamine and 30 mL of HI were mixed and stirred for two hours at 0°C . Red color precipitates were recovered by solvent evaporation using rotary evaporator at 60°C . This precipitate was rinsed with diethyl ether until the red color of the precipitate changed from red to yellow to colorless and then recrystallized in ethanol. The white crystalline powder of Methyleammonium Iodide (MAI) was dried in a vacuum oven at 60°C for 24 hours [23-27]. MAPbI_3 perovskite precursor solution was prepared in a nitrogen filled glovebox by dissolving 461 mg of PbI_2 , 159 mg of MAI, 0.5 mL of DMSO and 0.5 mL of Daymethyle formamide (DMF) under stirring overnight. $\text{MAPbI}_{3-x}\text{Cl}_x$ perovskite precursor solution was prepared by dissolving 461 mg of PbI_2 , 159 mg of MAI, 35 mg of PbCl_2 (10wt%), 0.5 mL of DMSO and 0.5 mL of DMF under stirring overnight. The prepared $\text{MAPbI}_{3-x}\text{Cl}_x$ perovskite solution was filtered by using a syringe filter prior to be used for the deposition of films.

2.4. Characterization techniques

The optical properties of the prepared perovskite and different layers were obtained by UV-visible spectroscopy (spectrophotometer, Thermo Scientific 600, USA). X-ray diffraction of GO was obtained using (X-ray 7000 Shimadzu, Japan). Photoluminescence spectra were recorded for the perovskite layer deposited on a glass and on the prepared HTLs at an excitation wavelength of 420 nm using (spectrophotometry Perkin Elmer L55, USA). The surface of different films was investigated using scanning electron microscopy (SEM "JEOL JSM-6360 LA", Japan) to study the morphology and the homogeneity of the surface. The structural identifications were confirmed by the FTIR spectroscopy using Fourier transform infrared spectrophotometer (Spectrum BX 11- LX 18-5255 Perkin Elmer). The spectra were recorded in the wavenumber range of $400\text{-}4000\text{ cm}^{-1}$. To obtain the FTIR spectra the powder from each layer was grinded with KBr powder. The J-V curves of the fabricated solar cells were measured using Metrohm Auto lab potentio state attached with calibrated halogen lamp with an intensity power of 80mW/cm^2 .

2.5. PSCs fabrication

The cleaning steps were carefully carried out these steps included sonication of the substrates in various solvents starting from acetone for 5 to 10 minutes, then Isopropanole (IPA) for 10 minutes and acetone again for 10 minutes. The FTO substrates were immediately rinsed by flow of nitrogen to dry and avoid adhesion of impurities on the wet surfaces.

The cell without passivation consists of FTO/BL-TiO₂/MP-TiO₂/MAPbI₃/CCE heterostructure as indicated in Fig.1. On top of the cleaned substrates the TiO₂ compact layer was deposited at 2000 rpm spincoating speed for 30 second and anealed at 450 °C for 30 minutes. Afterthat, the TiO₂ mesoporous layer was deposited on the top of the blocking layer at 4000 rpm for 30 s and anealed again at 450 °C for 30 min. After cooling to room temperature a mesoscopic CCE was deposited by doctor blade method and anealed at 450 °C for 30 min [28-29]. Finally a 30 µl of MAPbI₃ precursor was deposited and infiltrated through the mesoscopic carbon layer at 2000 rpm for 30 s and followed by drying at 100 °C for 30 min on a hot plate.

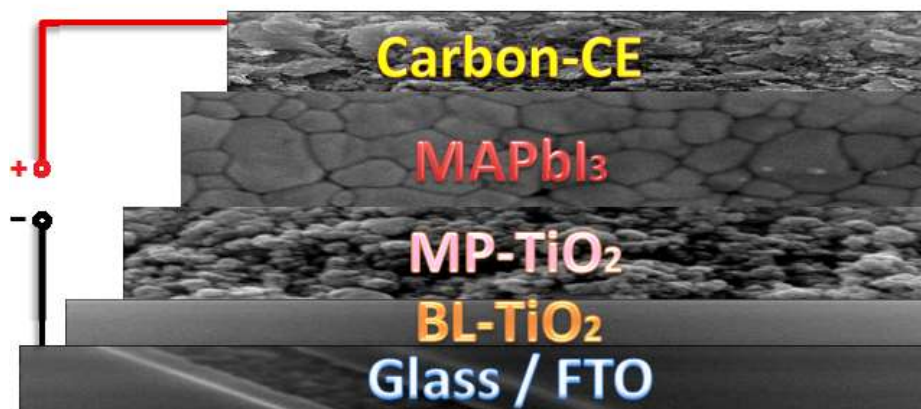


Fig. (1): Schematic diagram of the fabricated PSCs based on the mesoporous configuration of FTO/BL-TiO₂/MP-TiO₂/Active layer/CCE.

The PSCs with a self passivation (FTO/BL-TiO₂/MP-TiO₂/MAPbI_{3-x}Cl_x/CCE) structure was fabricated. The third type of cell was based on (FTO/BL-TiO₂/mP-TiO₂/MAPbI_{3-x}Cl_x/CB/CCE) to study the effect of surface passivation. To have higher performance with adding CB as the antisolvent solution very quickly during spincoating process on the last active layer [30]. The fourth fabricated PSC has the three types of passivation and involves FTO/BL/TiO₂/MP-TiO₂/TiCl₄/MAPbI_{3-x}Cl_x/CB/CCE structure to study the effect of interface passivation. In this cell the dense and mesoporous TiO₂ was deposited as previously mentioned and when the substrate with the TiO₂ films was treated in 0.04 M TiCl₄ solution at 70°C for 10 min, followed

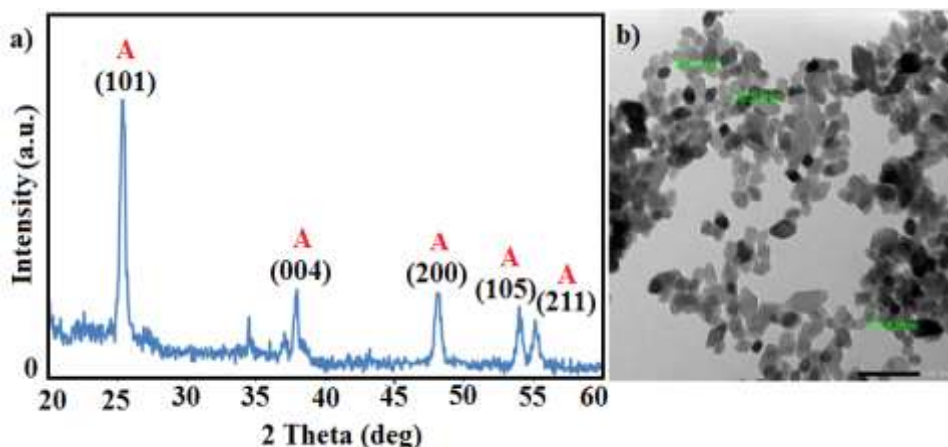


Fig. (2): (a) XRD pattern for TiO₂ nanoparticles films prepared on glass/FTO substrate and (b) TEM micrographs of the pattern of TiO₂ nanoparticles.

by rinsing with DI-water and ethanol and dried at 100°C for 10 min. Then, the TiO₂ film was annealed again at 500 °C for 30 min before the deposition of the perovskite layer [31, 32]. CCE paste was synthesized by mixing 2 g of carbon black powder with 6 g of graphite powders in 30 mL α -terpineol solution, and then 1 g of ZrO₂ powder and 1 g of EC were diluted with 37.5 mL of ethanol to obtain homogenous solution and followed by stirring for 2 hours.

3. Results and Discussion

3.1. Structure and morphology of TiO₂ nanoparticles

At the first, the TiO₂ nanoparticles were characterized by using XRD pattern as displayed in Fig. (2.a). The diffraction peaks are used at ($2\Theta = 25.3^\circ$, 37.9° , 48.1° , 54.8° , and 55.1°) corresponding to (1 0 1), (0 0 4), (2 0 0), (1 0 5), and (2 1 1) planes of anatase, respectively [33, 34]. There were no other detectable peaks corresponding to the rutile crystal structure. This confirms that the TiO₂ nanoparticles are in the pure anatase crystal structure. In Fig. (2.b) the TEM micrograph shows that the average size of the nanoparticles is less than 30 nm and that the nanoparticles appeared to be relatively homogeneous and uniform in size albeit fairly agglomerated.

3.2. Optical property of passivated perovskite films

To understand the optical absorbance of MAPbI₃ film and the effect of Cl element on the absorbance of MAPbI_{3-x}Cl_x film, UV-Vis absorption is measured in the 300-850 nm. The absorption edge for MAPbI_{3-x}Cl_x film at approximately 750 nm is observed and a slight green shift compared with 748 nm for MAPbI₃ film as shown in Fig. 3.a. The high absorbance of the perovskite film in the UV-

visible range showed that the film was excellent capability of wide spectrum response. To explore the change in the optical band gap, the energy band (E_g) was calculated according to Tauc's plot. The Tauc's plot shows that the E_g of MAPbI₃ film is approximately 1.45 eV compared with MAPbI_{3-x}Cl_x that showing 1.49 eV as depicted in inset of Fig. (3a) [14].

The antisolvent treatment can be control the morphology of the PSC films and influence on structural and optical properties for MAPbI_{3-x}Cl_x PSC films. To understand the role of CB as an antisolvent onto the deposited MAPbI_{3-x}Cl_x film by comparing the absorption spectra of MAPbI_{3-x}Cl_x and the new composite MAPbI_{3-x}Cl_x PSC films with non-polar solvent treatment as shown in Fig. 3.b. A slight red shift to 758 nm of MAPbI_{3-x}Cl_x+CB film is observed.

The high absorbance of the perovskite film in the UV-visible range enables the film with the excellent capability of wide spectrum response. To explore the change in the optical band gap, we calculate the energy band (E_g) according to the reflection and transmission through the Tauc's plots. In inset of Fig. 3.b the Tauc plot shows that the E_g of MAPbI_{3-x}Cl_x film is approximately 1.49 eV compared with the passivated MAPbI_{3-x}Cl_x with CB and showing 1.54 eV. The results demonstrate the enhancement of photoelectric performance of the passivated MAPbI_{3-x}Cl_x with CB film in the ultraviolet spectrum because the adding of CB in MAPbI_{3-x}Cl_x makes the cell surface more homogenous and pin hole free and enhance the absorbed incident light.

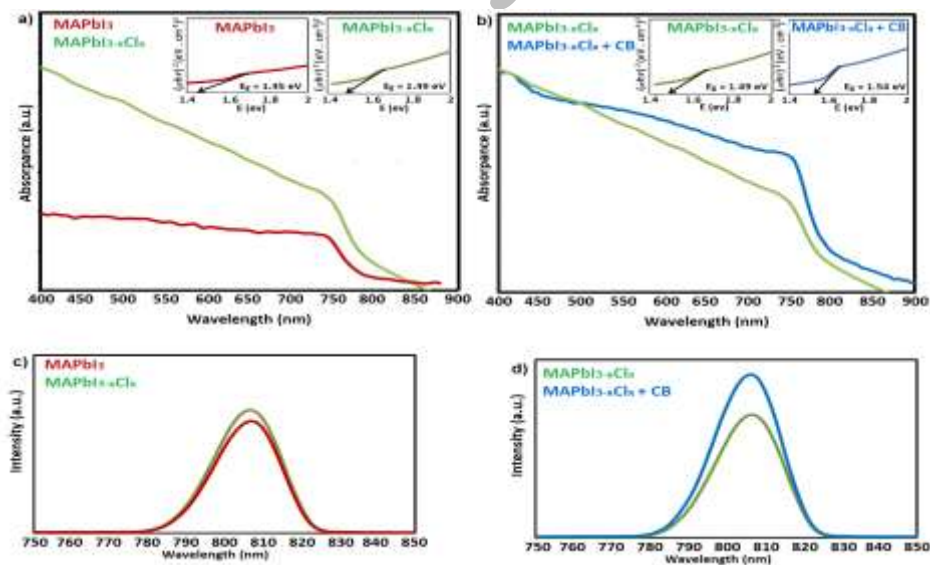


Fig. 3: a) Optical absorption spectra for the MAPbI₃ and MAPbI_{3-x}Cl_x thin film, a) inset $(\alpha h\nu)^2$ vs. $h\nu$ curves for MAPbI₃ and MAPbI_{3-x}Cl_x thin films, b) Optical absorption spectra for the MAPbI_{3-x}Cl_x and MAPbI_{3-x}Cl_x+CB thin film, b) inset $(\alpha h\nu)^2$ vs. $h\nu$ curves for MAPbI_{3-x}Cl_x and MAPbI_{3-x}Cl_x+CB thin films.

inset $(\alpha h\nu)^2$ vs. $h\nu$ curves for $\text{MAPbI}_{3-x}\text{Cl}_x$ and $\text{MAPbI}_{3-x}\text{Cl}_x + \text{CB}$ thin films, c) PL spectra of the MAPbI_3 and $\text{MAPbI}_{3-x}\text{Cl}_x$ thin films and d) PL spectra of $\text{MAPbI}_{3-x}\text{Cl}_x$ without CB treatment and $\text{MAPbI}_{3-x}\text{Cl}_x$ treated with CB thin films

Since the gap energy of the passivated $\text{MAPbI}_{3-x}\text{Cl}_x$ with CB film is greater, this means that the probability of charge recombination is less. It is concluded that the active layer of $\text{MAPbI}_{3-x}\text{Cl}_x$ passivated with CB overcomes the problem of charge recombination. The results demonstrate the enhancement of photoelectric performance of the $\text{MAPbI}_{3-x}\text{Cl}_x$ film in the ultraviolet spectrum because the doping of Cl in MAPbI_3 reduces the lattice symmetry and thus increases the material band gap. Since the gap energy of $\text{MAPbI}_{3-x}\text{Cl}_x$ film is greater, the probability of charge recombination is less.

The variations of Photoluminance (PL) intensity with wavelength for MAPbI_3 and $\text{MAPbI}_{3-x}\text{Cl}_x$ are presented in Fig. 3c. The PL spectra show a slight green-shift with chloride incorporation, which is consistent with previous report. Compared to the MAPbI_3 , the green-shift in the mixed perovskite of $\text{MAPbI}_{3-x}\text{Cl}_x$ may be related to incorporation of chloride into the MAPbI_3 crystal lattice, which reduces the lattice symmetry and thus increases the material band gap [27]. The excitation intensity controls the density of photoexcited electrons and holes, which governs the behavior of these carriers. Each electron-hole recombination mechanism has a distinct functional dependence on carrier density. The MAPbI_3 layer shows lower PL peak intensity, indicating the lower excitation and higher recombination rate. It confirms that the mixing by Cl produces more excitation and reduces the charge recombination at the interfaces [35]. When the $\text{MAPbI}_{3-x}\text{Cl}_x$ thin layer was treated by CB, the PL spectrum is shown in Fig. 3. d. The $\text{MAPbI}_{3-x}\text{Cl}_x$ film without CB treatment has a lower PL peak intensity, indicating the lower excitation and higher recombination rate than those appearing when the $\text{MAPbI}_{3-x}\text{Cl}_x$ thin layer was treated by CB. The PSCs films have totally different surface morphologies with and without the non-polar solvent treatment in the previous studies [36-38]. The PSC film without the CB washing had very poor surface coverage, which can cause decrease in the absorption property compared with fully covered film.

To improve the properties of final cell, another layer the electron transport layer (MP- TiO_2) is inserted. In order to make sure that the charge does not overlap again throughout the cell, the charge transfer layer must be treated because of its large gaps, and this treatment is made by depositing a very small thickness layer of the diluted TiCl_4 solution. To gain insight into the influence of TiCl_4 treatment on the optical properties of TiO_2 , we performed a transmittance measurement. The quality of perovskite films directly affects the device performance of PSCs; therefore, to investigate the effect of post-treatment of TiO_2 on the deposition of the perovskite film, we deposited perovskite thin films on top of the TiO_2 films with TiCl_4 treatment. UV-V light transmission was measured in

the 300-900 nm range by a UV-visible spectrophotometer. As depicted in Fig.(4) after treated with TiCl_4 , the transmittances of TiO_2 substrates were slightly lower than the control sample.

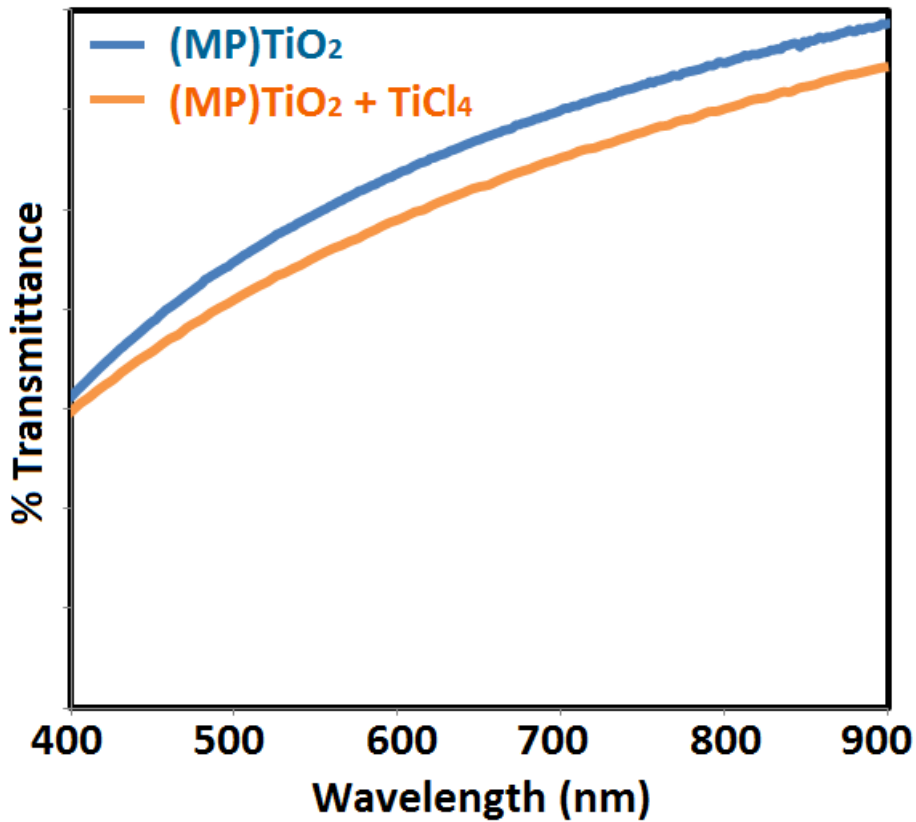


Fig. (4): UV-Vis absorption curves of the M-TiO₂ and M-TiO₂ + TiCl₄ thin film.

3.3. Structural, crystalline and morphological properties of passivated perovskite films.

To gain insight into the effects of the PbCl_2 additive on the crystal structure of the perovskite material, XRD data collected for the diffraction patterns of the films are represented in Fig. 5 (a, b). From the data of Fig. (5.b), it is noted that no peak from PbCl_2 is observed in the XRD patterns indicating that the added PbCl_2 is completely consumed in the reaction with MAI to either form PbI_2 or MAPbCl_3 . The existence of PbI_2 in 10% PbCl_2 - $\text{MAPbI}_{3-x}\text{Cl}_x$ film is attributed to the reaction of MAI with PbCl_2 rather than PbI_2 . As a result, there is insufficient MAI to react with PbI_2 , leading to the residues of PbI_2 in perovskite film [14]. Yu et al. [39] reported that the several reaction processes are involved in the formation of a film by these mixed solutions, and Cl elements slow down the formation of $\text{MAPbI}_{3-x}\text{Cl}_x$ crystal. Meanwhile, the excess of PbI_2 in the perovskite film at grain boundaries is beneficial because it forms an energy barrier that hinders leakage of both electrons and the holes from active layer for recombination [40].

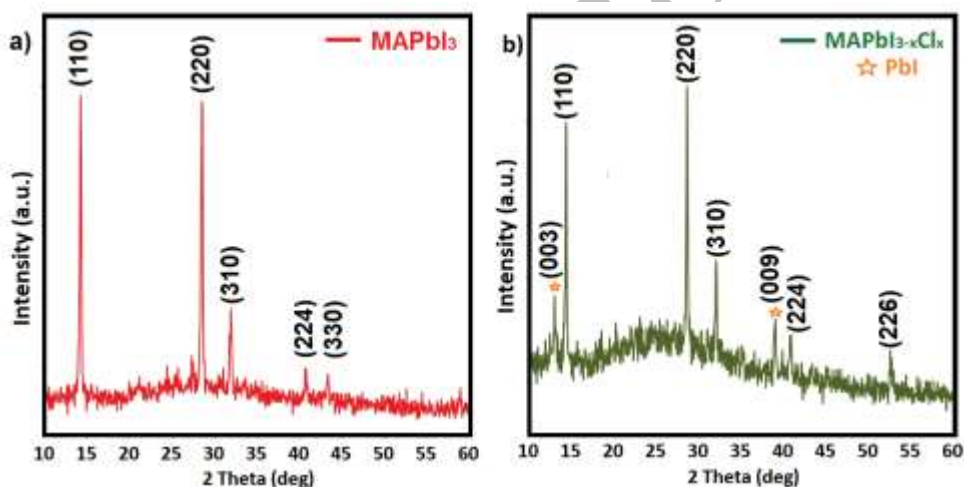


Figure (5) XRD patterns of a) MAPbI_3 and b) $\text{MAPbI}_{3-x}\text{Cl}_x$ thin film.

By comparing the XRD patterns, it is found that the presence of peaks at 14.2° (110), 28.5° (220), 31.9° (310), 40.55° (224) and 43.25° (330) indicates the successful formation of MAPbI_3 [41]. The results show that the (110) and (220) peaks are very strong compared to the other peaks, demonstrating better crystallization of perovskite film in these directions which is preferred for photovoltaic performance [42].

As shown in Fig. (5a and 5b) these peaks are shifted to 14.25° (110), 28.5° (220), 31.95° (310), 40.74° (224) and 52.45° (226) for the $\text{MAPbI}_{3-x}\text{Cl}_x$ [43]. This shift is slightly larger due to the inclusion of Cl ion into the crystal lattice of MAPbI_3 . The appearance of series of new diffraction peaks are in good agreement with literature on the tetragonal phase of the perovskite [44]. Furthermore, the figure shows that same PbI_2 in the $\text{MAPbI}_{3-x}\text{Cl}_x$ precursor appears at 12.9° (003) and 38.9° (009) and this unreacted PbI_2 passivates grain boundaries which generally worked as recombination centers.

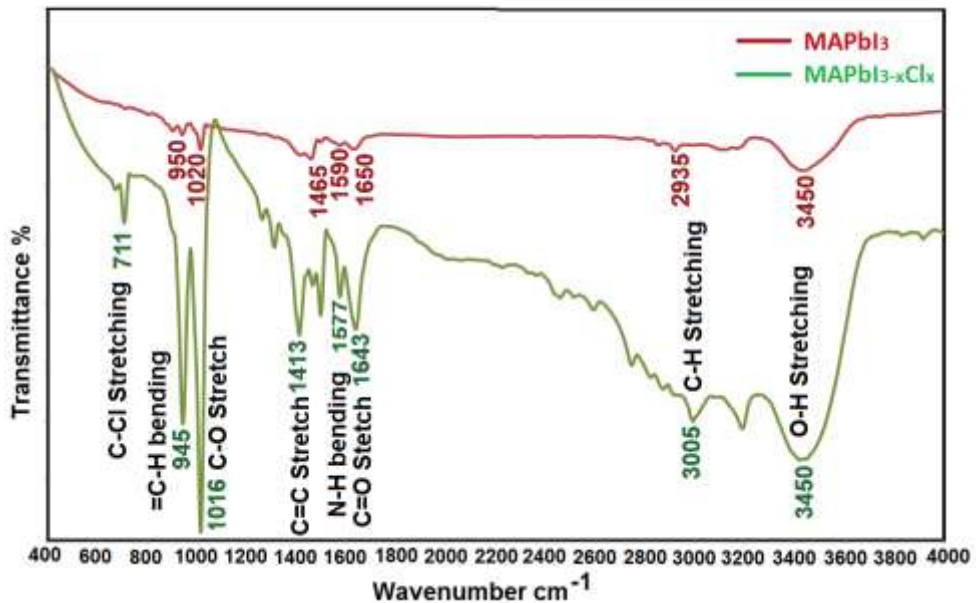


Figure (6) FTIR spectra of the MAPbI_3 and $\text{MAPbI}_{3-x}\text{Cl}_x$ thin film.

The chemical structures of $\text{CH}_3\text{NH}_3\text{PbI}_3$ and $\text{CH}_3\text{NH}_3\text{PbI}_{3-x}\text{Cl}_x$ thin layer were characterized by using FTIR and the spectra are shown in Fig.6. The spectra show that the characteristic peaks are slightly different from the other two types of perovskite materials. The wide band around 3450 cm^{-1} in the two structures is due to the hydroxyl radical O-H stretching (due to the decomposition process of perovskites), the peaks of 2935 cm^{-1} of $\text{CH}_3\text{NH}_3\text{PbI}_3$ and 3005 cm^{-1} of $\text{CH}_3\text{NH}_3\text{PbI}_{3-x}\text{Cl}_x$ is of the C-H stretch, the peaks appeared at 1643 cm^{-1} for $\text{MAPbI}_{3-x}\text{Cl}_x$ was shifted to 1650 cm^{-1} for MAPbI_3 as it is expected that the C=O bond strength in the PbI_2 -MAI-DMF and PbCl_2 -MAI-DMF complex should be decreased due to the interaction with the Lewis acids MA^+ , Pb^{2+} and PbCl_2^{2+} . The peaks appeared at 1577 cm^{-1} to 1590 cm^{-1} of N-H bend, the peaks 1413 cm^{-1} , 1465 cm^{-1} of C=C stretch, the peaks 1016 cm^{-1} and 1020 cm^{-1} of C-O stretch are

observed for MAPbI₃. The peak at 945 cm⁻¹ is shifted to 950 cm⁻¹ of =C-H bending and are assigned to the stretching mode of NH₃⁺/CH₃ ions rocking in CH₃NH₃PbI_{3-x}Cl_x and CH₃NH₃PbI₃. For MAPbI_{3-x}Cl_x the peak at 711 cm⁻¹ of C-Cl stretch was recorded. The differences in the assigned vibrational modes result from PbCl₂ and PbI₂.

The shifts in the vibrations and the change in the functional groups peaks broadening observed in the spectra are attributed to the formation of the two different perovskites. High transmittance at a frequency means there are few bonds to absorb that "color" or light in the sample, low transmittance means there is a high population of bonds which have vibrational energies corresponding to the incident light [45-47].

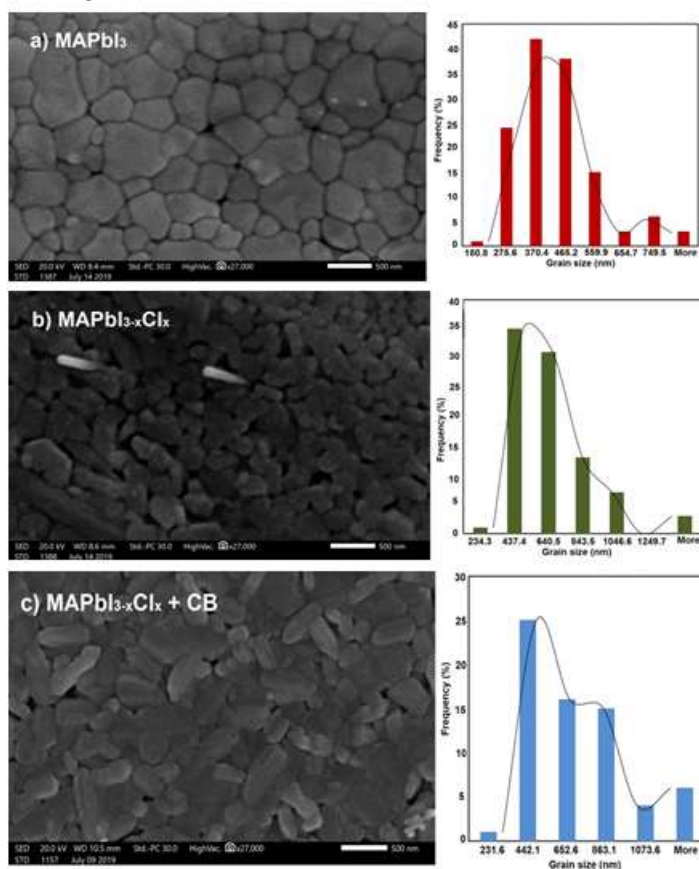


Fig. (7): SEM images of (a) MAPbI₃(b) MAPbI_{3-x}Cl_x and (c) MAPbI_{3-x}Cl_x + CB thin film.

The morphological changes in the MAPbI₃, MAPbI_{3-x}Cl_x and MAPbI_{3-x}Cl_x with CB treatment perovskite films by using SEM were inspected as shown in Fig. (7 a, b, c), respectively, and The statistical histogram of grain size of perovskite thin films is demonstrated. It is noticed that the large variations in

crystallite size with islands of sub-micron size can be seen clearly all over the surface. The presence of the random structures, grain boundaries and pinholes on the surface increases the possibility of current leakage.

The surface of MAPbI_3 is uniform but there are pinholes, a lot of grain boundaries and the average of grain size is nearly 391.8 nm as shown in Fig. (7.a), but in Fig. (7.b) the new composited $\text{MAPbI}_{3-x}\text{Cl}_x$ PSC films produces less grain boundaries and the average of grain size is 537.4nm, The Cl-doped perovskite films show improved crystalline structure and morphology and decrease the grain boundaries. Comparing $\text{MAPbI}_{3-x}\text{Cl}_x$ with the non-polar solvent treatment, the PSC film without any treatment process showed bad surface coverage, but for the cases of the CB treatment Fig. 7.b shows good coverage and no pinholes. On the other hand, relatively irregular distribution in grain sizes was modulated to be regularly distributed crystallites, and much planar surface and larger grain sizes were observed that in average grain size 609.5 nm indicating the best crystalline quality for device performance. Larger grains reduce the recombination

probability of electron-hole pairs at the grain boundaries and defect points, leading to the improvement in transporting rate of photo generated carrier and high-performance device [27, 48, and 49]. To make sure that the charge does not recombine again throughout the cell, and to obtain the greatest cell performance we will go to the interface passivation method that depends on the electron transport layer (MP- TiO_2) to improve its surface properties, SEM images of the pristine and treated (MP- TiO_2) showed that a very thin layer of compact titanium covered the surface of TiO_2 nanoparticles and improved its morphology and decreased the pin holes as shown in Fig. (8a and 8b) and that agree with literature [50].

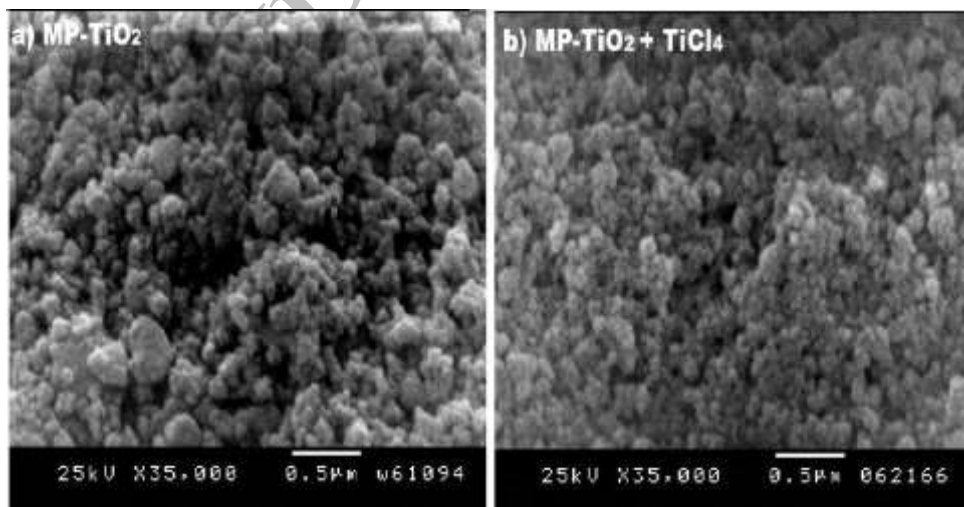


Fig. (8): SEM images of (a)MP- TiO_2 , (b)MP- $\text{TiO}_2 + \text{TiCl}_4$ thin film.

3.4. Effect of the passivation methods on the performance of PSCs

Although comparable PCEs are achieved in Figure (9), the reproducibility of the MAPbI₃ devices is poorer than that of the Cl-doped MAPbI_{3-x}Cl_x devices. To explore the benefits of the PbCl₂ additive to the perovskite precursor on the performance of solar cells, solar cells based on different structures from PbI and the other cell 10% PbCl₂ contents are fabricated and the parameters of J_{sc}, V_{oc}, FF and PCE are summarized in Table (1). PSCs based on FTO/BL/MP-TiO₂/MAPbI₃/C compared with FTO/BL-TiO₂/MP-TiO₂/MAPbI_{3-x}Cl_x/CCE (surface passivation) indicate that both cells have a single absorber layer of MAPbI₃ or MAPbI_{3-x}Cl_x. However, FTO/BL-TiO₂/MP-TiO₂/MAPbI_{3-x}Cl_x/CCE exhibits an improvement in the power conversion efficiency PCE by 40% and raises the J_{sc} by 90 % as compared to FTO/BL/MP-TiO₂/MAPbI₃/C, due to the substitution of PbI₂ by PbCl₂ in the precursor solution of MAPbI₃. The substitution improves the J_{sc} due to the high charge carrier transport properties of MAPbI_{3-x}Cl_x as indicated by PL. Where the higher mobility and more efficient transportation ability in the PSCs are responsible for the higher J_{sc} of PSCs [51, 52]. These observations imply that a better contact and charge transfer through cells with self-passivation method. The voids at the grain boundary increase the recombination process in the solar cell due to poor contact between the light absorbing particles. To overcome these defects, we add a new passivation material into the cell, which is an antisolvent solution from chlorobenzene.

Comparing FTO/BL/MP-TiO₂/MAPbI₃/C with FTO/BL-TiO₂/MP-TiO₂/MAPbI_{3-x}Cl_x/CCE, it is observed that the performance of FTO/BL-TiO₂/MP-TiO₂/MAPbI_{3-x}Cl_x/CB/CCE (surface passivation) is better than that of FTO/BL-TiO₂/MP-TiO₂/MAPbI_{3-x}Cl_x/CCE due to the improvement of the surface wetting properties of perovskite film after adding CB treatment the enhancement in the optical and morphological properties as proved by the absorption and SEM images in Figure (3) and (7). The typical MAPbI_{3-x}Cl_x with the antisolvent treatment cell has PCEs of 4.46% and higher in J_{sc}, V_{oc} and FF.

Table. (1): J_{sc}, V_{oc}, FF, and PCE of the cells without and with different passivation.

PSCs	J _{sc} (mA/cm ²)	V _{oc} (V)	FF	PCE %
FTO/BL/MP-TiO ₂ /MAPbI ₃ /C	16.8	0.227	0.215	1.64
FTO/BL-TiO ₂ /MP-TiO ₂ /MAPbI _{3-x} Cl _x /CCE	18.52	0.434	0.255	4.1
FTO/BL-TiO ₂ /MP-TiO ₂ /MAPbI _{3-x} Cl _x /CB/CCE	19.66	0.436	0.26	4.46
FTO/BL-TiO ₂ /MP-TiO ₂ /TiCl ₄ /MAPbI _{3-x} Cl _x /CB/CCE	20	0.56	0.29	6.5

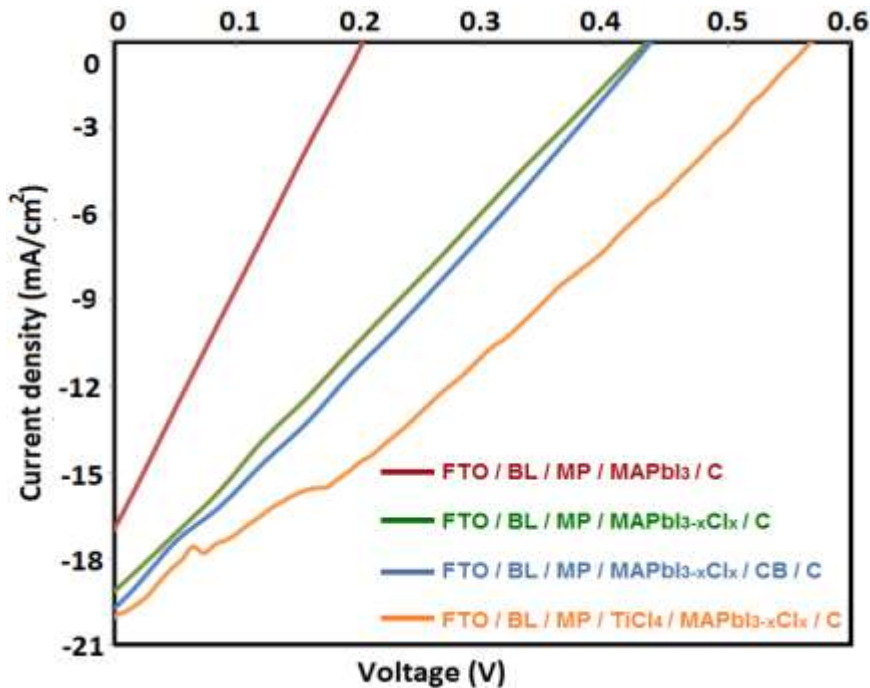


Fig. (9): J-V curves of the fabricated cells without out passivation media and the other with self, surface and interface passivation.

It is noted that FF of the PSCs has a low value (0.25-0.26) due to the high series resistance (R_s) between the perovskite/ TiO_2 and perovskite/carbon interfaces. The reduction in V_{oc} of FTO/BL/MP- TiO_2 /MAPbI₃/C and FTO/BL- TiO_2 /MP- TiO_2 /MAPbI_{3-x}Cl_x/CCE might be attributed to a reduction in the shunt resistance of the solar cell [56]. Moreover, there is another additional fabricated architecture consisted of FTO/BL- TiO_2 /MP- TiO_2 /TiCl₄/MAPbI_{3-x}Cl_x/CCE. By comparing its performance with cell-3 (surface passivation), it is exhibited the highest values in J_{sc} , V_{oc} , FF and the PCE as compared to the other cells. The FTO/BL- TiO_2 /MP- TiO_2 /MAPbI_{3-x}Cl_x/CB/CCE cell has the highest J_{sc} of 20 mA/cm^2 , FF of 0.29, and V_{oc} of 0.56 V and PCE of 6.5%.

4. Conclusion

This work indicated that different passivation techniques affected and improved the performance of the fabricated PSCs. The MAPbI_{3-x}Cl_x film without CB treatment had a lower PL peak intensity, indicating the lower excitation and higher recombination rate than the MAPbI_{3-x}Cl_x thin layer treated by CB. It was found that the maximum performance is of the fabricated and passivated PSCs with a structure of (FTO/BL/MP- TiO_2 /TiCl₄/MAPbI_{3-x}Cl_x/CB/CCE) where it has J_{sc} , V_{oc} , FF and efficiency of 20 mA/cm^2 , 0.56 V, 0.29 and 6.5 %, respectively.

Data Availability

The data that support the findings of this study are available from the corresponding author upon reasonable request.

Conflict of interest

The authors declare that there are no conflicts of interest.

References

1. Zhaoyi Wan, *Journal of Metals Research*, **35** (16), 2166-2189, (2020)
2. Jeon, N.J.; Noh, J.H.; Yang, W.S.; Kim, Y.C.; Ryu, S.; Seo, J.; Seok, S.I. *Nature*, **517**, 476–480, (2015).
3. Park, N.G. Perovskite solar cells: An emerging photovoltaic technology. *Materials Today*, **18**, 65–72, (2014).
4. Green, M.A.; Baillie, A.H.; Snaith, H.J. The emergence of perovskite solar cells. *Nature Photonics*, **8**, 506–514. (2014).
5. Qiliang Chen, Lianjie Zhang, Shaker Ebrahim, MoatazSoliman, Cheng Zhang, and Qiquan Qiao, *Polymer* **54**, 223-229, (2013).
6. A.H. Ip, L.N. Quan, M.M. Adachi, J.J. McDowell, J.X. Xu, D.H. Kim, E.H. Sargent, *Applied Physics Letters*, **106**, 143902, (2015)
7. Y.W. Li, Y. Zhao, Q. Chen, Y. Yang, Y.S. Liu, Z.R. Hong, Z.H. Liu, Y.T. Hsieh, L.Meng, Y.F. Li, Y. Yang, *Journal of the American Chemical Society*, **137**, 15540–15547, (2015).
8. J.X. Song, E.Q. Zheng, J. Bian, X.F. Wang, W.J. Tian, Y. Sanehira, T. Miyasaka, *Journal of Materials Chemistry A*, **3**, 10837-10844, (2015).
9. N. Arora, M.I. Dar, M. Abdi-Jalebi, F. Giordano, N. Pellet, G. Jacopin, R.H. Friend, S.M. Zakeeruddin, M. Grazel. *Nano Letters*, **16**, 7155–7162, (2016).
10. W.J. Ke, C.X. Xiao, C.L. Wang, B. Saparov, H.S. Duan, D.W. Zhao, Z.W. Xiao, P. Schulz, S.P. Harvey, W.Q. Liao, W.W. Meng, Y. Yu, A.J. Cimaroli, C.S. Jiang, K. Zhu, M. Al-Jassim, G.J. Fang, D.B. Mitzi, Y.F. Advanced *Materials*, **28**, 5214-5221, (2016).
11. P. Zhao, B. J Kim, H. S. Jung, *Materials Today Energy*, **7**, 267-286, (2018).
12. L. Etgar , P. Gao , Z. Xue , Q. Peng , A. K. Chandiran , B. Liu , M. K. Nazeeruddin , M. Grätzel, *Journal of American Chemical Society*, **134**, 17396–17399. (2012).
13. A. Mei , X. Li , L. Liu , Z. Ku , T. Liu , Y. Rong , M. Xu , M. Hu , J. Chen , Y. Yang , M. Grätzel , H. Han, *Science*, **345**, 295-298, (2014).
14. Hao Li, Dandan Yang, Ting Zhang, Peng Zhang, Feng Wang, Chaojie Qin, Ruihan Yang, Zhi David Chen, Shibin Li, *Journal of Materials Science*, **54**, 11556–11563, (2019).
15. P. D. Matthews, D. J. Lewis, P. O'Brien, *Journal of Materials Chemistry A*, **5**, 17135-17150, (2017).

16. M. L. Petrus, J. Schlipf, C. Li, T. P. Gujar, N. Giesbrecht, P. Müller-Buschbaum, M. Thelakkat, T. Bein, S. Hüttner, P. Docampo. *Advanced Energy Materials*, 7, 1700264, (2017).
17. Mustafa Aboulsaad, Ayman El Tahan, Moataz Soliman, Said El-Sheikh, Shaker Ebrahim, *Journal of Materials Science: Materials in Electronics*, 30:19792–19803, (2019).
18. M. Abdi-Jalebi, M.I. Dar, A. Sadhanala, S.P. Senanayak, M. Grätzel, R.H. Friend, *Journal of Visualized Experiments*, 121, 55307, (2017).
19. Fan, H., Yang, Z., Ren, X., Yin, M., Gao, F., & Liu, *AIP Advances*, 6, 015314, (2016).
20. More, V., Shivade, V., & Bhargava, P. *Transactions of the Indian Ceramic Society*, 75, 59-62, (2016).
21. Ito, S., Murakami, T. N., Comte, P., Liska, P., Grätzel, C., Nazeeruddin, M. K., & Grätzel, M. *Thin solid films*, 516, 4613-4619, (2008).
22. Wang, X., Fang, Y., He, L., Wang, Q., & Wu, T. *Materials Science in Semiconductor Processing*, 27, 569-576, (2014).
23. Xiao, Z., Bi, C., Shao, Y., Dong, Q., Wang, Q., Yuan, Y.,...& Huang, J. *Energy & Environmental Science*, 7, 2619-2623, (2014).
24. Duan, B., Ren, Y., Xu, Y., Chen, W., Ye, Q., Huang, Y. & Dai, S. *Inorganic Chemistry Frontiers*, 4, 473-480, (2017).
25. M. Habib, M. Feteha, M. Soliman, A. Abdel Motagaly, S. El-Sheikh, and Sh. Ebrahim, *Journal of Materials Science: Materials in Electronics*, 31, 18870 – 18882, (2020)
26. Ren, Y. K., Ding, X. H., Wu, Y. H., Zhu, J., Hayat, T., Alsaedi, A. & Dai, S. Y. *Journal of Materials Chemistry A*, 5, 20327-20333, (2017).
27. N.D. Pham, V.T. Tiong, P. Chen, L. Wang, G.J. Wilson, J. Bell, H. Wang, *Journal of Materials Chemistry A*, 5, 5195-5203, (2017).
28. Zhang, L., Liu, T., Liu, L., Hu, M., Yang, Y., Mei, A., & Han, H. *Journal of Materials Chemistry A*, 3, 9165-9170, (2015).
29. Zhao, P., Han, M., Yin, W., Zhao, X., Kim, S. G., Yan, Y. Jung, H. S. *ACS applied materials & interfaces*, 10, 10132-10140, (2018).
30. Ban-Suk Park, Seojun Lee, Saemon Yoon, Tae-Jun Ha, Dong-Won Kang, *Applied Surface Science*, 427, 421-426, (2017).
31. Zhang, H., Shi, Y., Yan, F., Wang, L., Wang, K., Xing, Y., ...& Ma, T. *Chemical Communications*, 50, 5020-5022, (2014).
32. Roose, B., Gödel, K. C., Pathak, S., Sadhanala, A., Baena, J. P. C., Wilts, B. D. & Abate, A. *Advanced Energy Materials*, 6, 1501868, (2016).
33. W. Li, S. Shah, C. P. Huang, O. Jung, and C. Ni. *Materials Science and Engineering B*, 96, 247–253, (2002).
34. X. W. Zhang, M. H. Zhou, and L. C. Lei. *Catalysis Communications*, 7, 427–431, (2006).
35. Timothy H. Gfroerer, *Encyclopedia of Analytical Chemistry: Applications, Theory and Instrumentation* 9209–9231, (2006).

36. N. Sakai, S. Pathak, H.-W. Chen, A.A. Haghghirad, S.D. Stranks, T. Miyasaka, H.J. Snaith, *Journal of Materials Chemistry A*, **4**, 4464-4471, (2016).
37. Tarek M. Abdel-Fattah, Shaker Ebrahim, MoatazSoliman, and Mostafa Hafez, *ECS Journal of Solid State Science and Technology*, **2** (6) M13-M16 (2013).
38. K.-F. Lin, S.H. Chang, K.-H. Wang, H.-M. Cheng, K.Y. Chiu, K.-M. Lee, S.-H. Chen, C.-G. Wu, *Solar Energy Materials and Solar Cells*, **141**, 309-314, (2015).
39. Yu H, Wang F, Xie F, Li W, Chen J, Zhao N, *Advanced Functional Materials*, **24**, 7102-7108, (2015),
40. Bi D, Tress W, Dar MI et al. *Science Advances*, **2**, e1501170-e1501170, (2016).
41. C. Huang, N. Fu, F. Liu, L. Jiang, X. Hao, H. Huang, *Solar Energy Materials and Solar Cells*, **145**, 231-237, (2016).
42. Guo, X., McCleese, C., Kolodziej, C., Samia, A. C., Zhao, Y., &Burda, C, *Dalton Transactions*, **45**, 3806-3813, (2016)
43. *Journal of Materials Chemistry A*, **3**, 20849–20862, (2015),
44. *Abdelmagid, A., El Tahan, A., Habib, M., Anas, M., Soliman, M., Synthetic Metals*, **259**, 116232, (2020).
45. Cho, K. T., Paek, S., Grancini, G., Roldán-Carmona, C., Gao, P., Lee, Y., &Nazeeruddin, M. K, *Energy & Environmental Science*, **10**, 621-627, (2017).
46. Liu, D., Liu, C., Wu, L., Li, W., Chen, F., Xiao, B. &Feng, L. *RSC Advances*, **6**, 51279-51285, (2016).
47. XinGuo, Christopher McCleese, Charles Kolodziej, Anna C. S. Samia, Yixin Zhao, Clemens Burda, *Dalton Transactions*, **45**, 3806-3813, (2016).
48. Song, Z., Wathage, S. C., Phillips, A. B., Tompkins, B. L., Ellingson, R. J., &Heben, M. J, *Chemistry of Materials*, **27**, 4612-4619, (2015).
49. Li, Z., Kolodziej, C., McCleese, C., Wang, L., Kovalsky, A., Samia, A. C., &Burda, C, *Nanoscale Advances*, **1**, 827-833, (2019).
50. MojtabaAbdi-Jalebi, M. Ibrahim Dar, AdityaSadhanala, Satyaprasad P. Senanayak, Fabrizio Giordano, Shaik Mohammed Zakeeruddin, Michael Grätzel, Richard H. Friend, *J. Phys. Chem. Lett.*, **7**, 16, 3264–3269, (2016)
51. Unger EL, Hoke ET, Bailie CD, Nguyen WH, Bowring AR, Heumuller T, Christoforod MG, McGehee MD. *Energy & Environmental Science*, **7**, 3690–3698, (2014).
52. Wehrenfennig, C., Eperon, G. E., Johnston, M. B., Snaith, H. J., &Herz, L. M., *Advanced materials*, **26**, 1584-1589, (2014).